Nano Research
2022, 15(3): 1959–1965

ISSN 1998-0124 CN 11-5974/O4
https://doi.org/10.1007/s12274-021-3843-8

Research Article

RuO_2 clusters derived from bulk $SrRuO_3$: Robust catalyst for oxygen evolution reaction in acid

Muwei Ji[1,2,§], Xin Yang[3,§], Shengding Chang[3,§], Wenxing Chen[4,§], Jin Wang[1,3,§] (✉), Dongsheng He[5], Yao Hu[3], Qian Deng[3], You Sun[3], Bo Li[3], Jingyu Xi[3], Tomoaki Yamada[6], Jiatao Zhang[4], Hai Xiao[7], Caizhen Zhu[2], Jia Li[3] (✉), and Yadong Li[7] (✉)

[1] *College of Materials Science and Engineering, Shenzhen University, Shenzhen 518060, China*
[2] *Institute of Low-Dimensional Materials Genome Initiative, College of Chemistry and Environmental Engineering of Shenzhen University, Shenzhen 518060, China*
[3] *Tsinghua Shenzhen International Graduate School, Tsinghua University, Shenzhen 518055, China*
[4] *Beijing Key Laboratory of Construction Tailorable Advanced Functional Materials and Green Applications, School of Materials Science and Engineering, Beijing Institute of Technology, Beijing 100081, China*
[5] *Materials Characterization and Preparation Center, Southern University of Science and Technology, Shenzhen 518055, China*
[6] *Department of Energy Engineering, Nagoya University, Furo-cho, Chikusa-ku, Nagoya 464-8603, Japan*
[7] *Department of Chemistry, Tsinghua University, Beijing 100084, China*
[§] *Muwei Ji, Xin Yang, Shengding Chang, Wenxing Chen, and Jin Wang contributed equally to this work.*

Received: 28 June 2021 / **Revised:** 19 August 2021 / **Accepted:** 25 August 2021

ABSTRACT

Developing highly efficient oxygen evolution reaction (OER) catalyst for the acidic corrosive operating conditions is a challenging task. Herein, we report the synthesis of uniform RuO_2 clusters with ~ 2 nm in size via electrochemical leaching of Sr from $SrRuO_3$ ceramic in acid. The RuO_2 clusters exhibit ultrahigh OER activity with overpotential of ~ 160 mV at 10 $mA\cdot cm_{geo}^{-2}$ in 1.0 M $HClO_4$ solution for 30-h testing. The extended X-ray absorption fine structure measurement reveals enlarged Jahn-Teller distortion of Ru-O octahedra in the RuO_2 clusters compared to its bulk counterpart. Density function theory calculations show that the enhanced Jahn-Teller distortion can improve the intrinsic OER activity of RuO_2.

KEYWORDS

oxygen evolution reaction, RuO_2 cluster, electrochemical leaching, acid solution

1 Introduction

Oxygen evolution reaction (OER) is a crucial process in energy conversion and storage technologies such as (photo-)electrochemical water-splitting and regenerative fuel cells [1–6]. In recent years, diverse types of OER catalysts, including noble-metal/noble-metal oxide [7–8], nickle oxides/hydroxides [7, 9–10], cobalt oxides [10, 11], metal organic frameworks [12], C_3N_4 [13, 14], and their hybrid materials [15–20] have been explored. The structure of catalysts, such as porous framework, heterostructure, and so on, were designed and fabricated for enhancing the activity [21–26] and multiple functionization [27–29]. Although most of these studied catalysts were found to exhibit enhanced OER activity in alkaline electrolytes, they usually showed higher overpotential and lacked of stability in acid solution [30–34]. For a long time, ruthenium and iridium oxides [35–39], which usually require overpotential of > 320 mV to reach a current density of 10 $mA\cdot cm_{geo}^{-2}$ [37, 40–42], were regarded as the most applicable OER catalysts in acid. An $IrO_x/SrIrO_3$ catalyst formed by Sr leaching from surface layers of $SrIrO_3$ thin films during OER testing, was reported to demonstrate excellent OER catalytic activity in acid, with 270–290 mV overpotential at 10 $mA\cdot cm_{geo}^{-2}$ for 30 h in 0.5 M H_2SO_4 solution [40]. Pyrochlore yttrium ruthenate ($Y_2Ru_2O_{7-\delta}$) was shown to exhibit high stability in 0.1 M perchloric acid solution and a low onset overpotential of 190 mV for OER [43]. Nevertheless, it required > 300 mV overpotential to reach a reasonable current density of 10 $mA\cdot cm_{geo}^{-2}$ [43]. As acidic working condition, for instance, in polymer electrolyte membrane (PEM) electrolysers, is favorable for OER due to high proton conductivity and limited side reactions, development of efficient and durable OER catalysts in acid is urgently required.

In the past few years, outstanding OER activity of $SrRuO_3$ (SRO) thin film or nanopowders has been noticed and attracted considerable attentions [44]. Nevertheless, very fast performance degradation of $SrRuO_3$ thin film and $SrRuO_3$ nanopowder at relatively large current density (e.g., at 10 $mA\cdot cm_{geo}^{-2}$) especially in acid [44–46], prevented the application of $SrRuO_3$ thin film or nanopowder as a stable OER electrode despite their high activity.

In this work, we report robust OER activity of RuO_2 clusters synthesized via a top-down strategy starting with a bulk $SrRuO_3$ ceramic pellet, with an overpotential of ~ 160 mV at 10 $mA\cdot cm_{geo}^{-2}$ in 1.0 M $HClO_4$ solution for 30-h testing. The uniform rutile RuO_2 clusters with ~ 2 nm in size are formed via electro-chemical

---

Address correspondence to Jin Wang, wangjin19@szu.edu.cn; Jia Li, li.jia@sz.tsinghua.edu.cn; Yadong Li, ydli@tsinghua.edu.cn

leaching of Sr from $SrRuO_3$ ceramic in acid. In contrast to the $SrRuO_3$ electrode, the RuO_2 clusters exhibit great improvement in both performance stability and chemical durability. Density functional theory (DFT) calculations were performed to understand the origin of the extremely high OER activity of RuO_2 clusters.

2 Experimental details

Chemicals: Commercial $SrRuO_3$ powder was purchased from Element Tech Material Co., Ltd. Poly(vinyl alcohol) (PVA) was purchased from Alfa Aesar Co., Ltd. $HClO_4$ was purchased from Macklin Co., Ltd. All the chemicals were used without further purification.

Preparation of $SrRuO_3$-ceramic electrode: $SrRuO_3$ (1.0 g) was mixed with PVA solution (5%, 50 μL) by grounding them together. The as-prepared $SrRuO_3$ powder (50 mg) was pressed into a pellet with 5 mm in diameter with a mould under 20 MPa for 10 s. The $SrRuO_3$ pellet was sintered at 1,200 °C for 10 h (Fig. S1(a) in the Electronic Supplementary Material (ESM)). The RuO_2 ceramic plate was prepared by following a similar method except sintered at 800 °C for 10 h. As illustrated in Fig. S1(b) in the ESM, $SrRuO_3$ ceramic (or RuO_2 ceramic) was pasted on a disk electrode by using Nafion solution (5%) mixed with conductive carbon to ensure both the mechanical and electrical contact. After being dried at room temperature, the $SrRuO_3$ ceramic electrode was further fixed on its side planes by epoxy resin. The as-prepared $SrRuO_3$ ceramic electrode was placed at room temperature for more than 24 h before measurement.

Preparation of RuO_2-cluster electrode: After 30-h chronopotentiometry (CP) measurement of $SrRuO_3$ ceramic electrode, the powders on the surface of ceramic electrode were collected and checked by X-ray diffraction (XRD) to confirm phase purity. For preparing RuO_2-cluster electrode with 0.5 $mg\cdot cm^{-2}$ loading which was subjected to linear sweep voltammetry (LSV) and CP test, 10 mg as-obtained RuO_2 clusters were dispersed in 1 mL solvent containing 900 μL isopropyl alcohol and 100 μL 5 wt.% nafion solution, and sonicated for more than 1 h to form a homogeneous ink. Then 10 μL of the diluted ink was dropped onto the Pt-disk electrode (0.196 cm^2 in area) and dried at room temperature for 24 h. To prepare a RuO_2-cluster electrode with 4.0 $mg\cdot cm^{-2}$ loading on sticky-carbon, the ink was dropped onto an electrode prepared via filling the mixture of carbon black and eicosane into an empty well (0.196 cm^2). Specifically, the empty hole of an rotating disk electrode was first filled with the mixture of conductive carbon black and eicosane (conductive carbon black:eicosane = 5:1 in weight) which had been heated to 50 °C for 10 min to make the wax melt and stirred to mix evenly in the melted state, under irradiation of an infrared lamp. RuO_2 clusters (10 mg) were dispersed in 100 μL solvent containing 90 μL isopropyl alcohol and 10 μL 5 wt.% Nafion solution, and sonicated for more than 1 h to form a homogeneous ink. Then 8 μL of as-prepared catalyst ink was loaded onto the flat carbon–wax region of the rotating disc electrode (RDE) center, and then dried up at room temperature for 24 h before electrocatalysis characterization.

Electro-chemical characterization: Electro-chemical characterization was carried out by using an electrochemical workstation CHI760E. An Ag/AgCl electrode in saturated KCl solution and a commercial Pt electrode (Wuhan GaossUnion, China) were used as a reference and a counter electrode respectively. $HClO_4$ solution (1.0 M) was used as electrolyte in the characterization. The according potential of reversible hydrogen electrode (RHE) was calculated following the equation

$$E_{\mathrm{RHE}} = E + 0.059\mathrm{pH} + 0.197\ \mathrm{V}$$

Structural characterization: The XRD patterns of samples were obtained with a Bruker D8 X-ray diffractometer with Cu Kα radiation (λ = 1.5418 Å). The surface morphology was characterized on a ZEISS SUPRA® 55 scanning electron microscope (SEM). High resolution transmission electron microscopy (HRTEM) study was carried out on a Tecnai G2 F30 equipped with an energy-dispersive X-ray spectroscopy (EDX) detector (Oxford X-Max 20). High-angle annular dark-field scanning transmission electron (HAADF-STEM) images were collected by using a Titan Cubed Themis G2 300 operating at 300 kV. X-ray photoelectron spectroscopy (XPS) was performed on a PHI-5000 Versaprobe II (Ulvac-Phi, Japan). The specific surface area of as-prepared RuO_2 clusters was measured with a Brunauer–Emmett–Teller (BET) analyzer (BELSORP-Max). Sr and Ru concentrations in the electrotyle electrode during OER test were measured by an inductively coupled plasma-atomic emission spectrometer (JY2000-2, HORIBA JOBINYVON). The X-ray absorption fine structure spectra (Ru K-edge) were collected at BL14W1 station in Shanghai Synchrotron Radiation Facility (SSRF, the storage ring was operated at 3.5 GeV with a maximum current of 250 mA).

3 Results and discussion

The RuO_2 clusters were derived as a result of the electrochemical leaching of bulk $SrRuO_3$ ceramic electrode under OER conditions in acid. $SrRuO_3$ ceramic was employed because $SrRuO_3$ thin film or nanopowder cannot endure OER at a relatively large current density or over a long-time scale [45, 47]. In addition, the intrinsic conductivity of $SrRuO_3$ permits the application of its ceramic monolithic wafer directly as an OER electrode.

$SrRuO_3$ ceramic pellet was prepared by a conventional ceramic processing method. The XRD pattern (Fig. S2 in the ESM) shows that the as-prepared $SrRuO_3$ ceramic consisted of a pure orthorhombic phase (JCPDS #43-0472). The SEM image (inset of Fig. S2 in the ESM) indicates good mechanical integrity of the sample with micron-sized grains. For the OER testing, the as-prepared $SrRuO_3$ ceramic was pasted onto a Pt disk electrode and glued with epoxy resin on its side surface, as shown in Fig. S1(b) in the ESM. The resistance between the exposed surface of the mounted $SrRuO_3$ and the Pt disk electrode was measured prior to the electrochemical testing. As indicated by the current–voltage (I–V) characteristic (Fig. S3 in the ESM), a good ohmic contact at the $SrRuO_3$ disk-electrode interface has been formed.

Figure 1(a) presents the polarization curve of $SrRuO_3$ ceramic electrode during OER in 1.0 M $HClO_4$ solution. It is shown that the OER onset potential of the $SrRuO_3$ ceramic electrode is 1.35 V_{RHE} (voltage vs. reversible hydrogen electrode) with according Tafel slope of 48.0 $mV\cdot dec^{-1}$ (inset of Fig. 1(a)). In comparison, the onset potential of the RuO_2 ceramic electrode is 1.51 V_{RHE} with a Tafel slope of 82.1 $mV\cdot dec^{-1}$ (inset of Fig. 1(a)), which is in agreement with the previous reports on the catalytic behavior of RuO_2 for OER in acid [41, 48]. Figure 1(b) shows the potential required to reach 10 $mA\cdot cm_{geo}^{-2}$ during a 30-h testing on the $SrRuO_3$ ceramic electrode. The overpotential η of the $SrRuO_3$ ceramic at 10 $mA\cdot cm_{geo}^{-2}$ constantly keeps ~ 160 mV over 30 h. The observed ultrahigh long-term activity of the $SrRuO_3$ ceramic electrode for OER in acid has never been reported in $SrRuO_3$ thin films or nanoparticle samples [45]. The OER testing on a ~ 50 nm thick $SrRuO_3$ film epitaxially grown on the (100) $SrTiO_3$ substrate (Fig. S4 in the ESM) in 1.0 M $HClO_4$ solution shows immediate severe degradation of activity during the chronopotentiometry measurement at 10 $mA\cdot cm_{geo}^{-2}$ (Fig. S5 in the ESM).

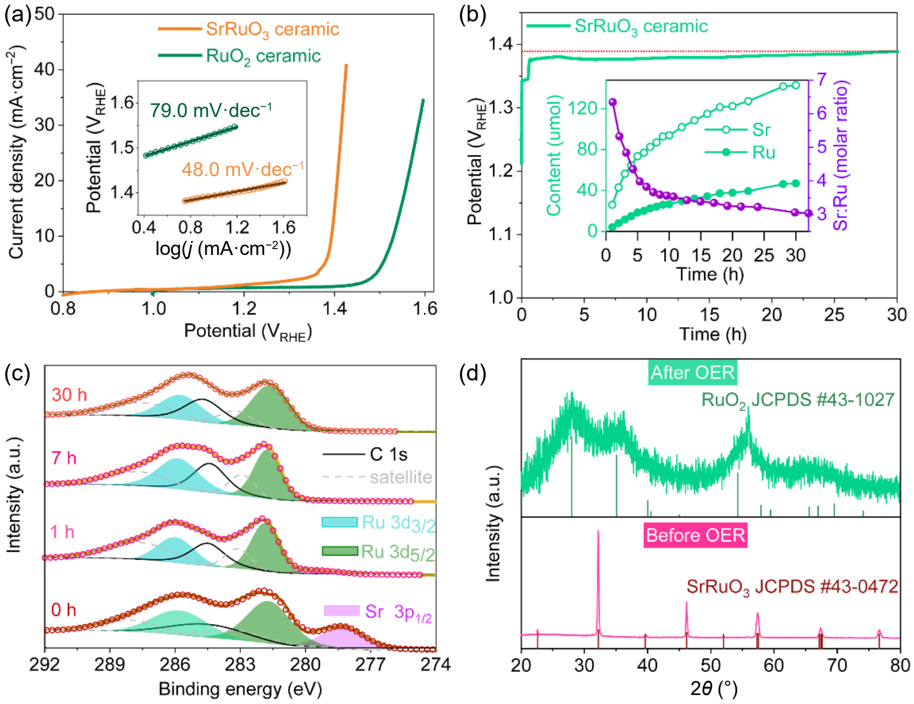

Figure 1 OER performance of $SrRuO_3$ ceramic electrode in acid and its leaching behavior. (a) Polarization curve of $SrRuO_3$ ceramic wafer. The inset is the according Tafel plot. (b) Potential required to reach 10 $mA{\cdot}cm_{geo}^{-2}$ for $SrRuO_3$ ceramic over 30-h OER testing. The dashed red line highlights the potential level corresponding to 160 mV overpotential as a guide to the eye. The inset shows the leached Sr and Ru at different time during 30-h OER testing according to the ICP analysis of the corresponding elements in the electrolyte (250 mL). (c) XPS of the surface of $SrRuO_3$ ceramic wafer after OER test at 10 $mA{\cdot}cm_{geo}^{-2}$. (d) XRD patterns of the $SrRuO_3$ ceramic wafer before OER test and of powders collected from the surface layer of $SrRuO_3$ wafer after 30-h OER test.

Considering the well-documented corrosion behaviour of $SrRuO_3$ thin film and nanoparticles under OER electrochemical conditions [46, 49], we tracked the loss of material of the $SrRuO_3$ ceramic electrode during the 30-h CP measurement by monitoring the amount of Sr and Ru elements in the electrolyte with the inductively coupled plasma (ICP) spectroscopy. As shown in the inset of Fig. 1(b), leaching of both Sr and Ru occurs and decreases gradually as the OER proceeds. The leaching rate of Sr is much faster than that of Ru, especially at the initial stage (Fig. S6 in the ESM). This corrosion rate indicates that the 30 nm $SrRuO_3$ film will be completely destroyed within hundreds of seconds in 1.0 M $HClO_4$ at a current density of 10 $mA{\cdot}cm_{geo}^{-2}$, which is exactly what has been experimentally observed (Fig. S5 in the ESM). The molar ratio between the leached Sr and Ru is also presented as a function of testing time (Fig. 1(b)), decreasing quickly from 6.3 to less than 3.5. The obvious deviation of the ratio between leached Sr and Ru from 1 indicates that the remaining Sr and Ru in the surface layer of the $SrRuO_3$ ceramic electrode cannot keep the same ratio as that in $SrRuO_3$ and thus surface reconfiguration should have occurred.

To further elucidate the surface evolution of $SrRuO_3$ ceramic electrode during OER in acid, XPS was conducted to examine the change of chemical composition of its surface layer. Figure 1(c) presents the XPS results of the $SrRuO_3$ ceramic electrode before and after 30-h CP testing at 10 $mA{\cdot}cm_{geo}^{-2}$ in 1.0 M $HClO_4$ solution. It is shown that the Sr $3p_{1/2}$ peak, which is present at 277.1 eV in the pristine $SrRuO_3$ ceramic with a chemical state of II [46], has completely disappeared after testing, indicating the loss of Sr in the surface layer during OER testing. The Ru element, which has $3d_{3/2}$ and $3d_{5/2}$ peaks located at 284.8 and 280.7 eV respectively in the pristine $SrRuO_3$ ceramic, remains in its IV chemical state after testing. The surface analysis of the $SrRuO_3$ ceramic electrode after 1-h and 7-h CP testing also shows the obvious loss of Sr and presence of Ru IV state (Fig. 1(c)). Powders collected from the surface layer after 30-h CP testing were inspected with XRD (Fig. 1(d)), from which a pure phase of rutile RuO_2 is unambiguously identified. HAADF-STEM and HRTEM images of the powders scratched from the surface of the $SrRuO_3$ ceramic electrode after 30-h CP testing (Figs. 2(a) and 2(b)) reveal that the powders consist of ~ 2 nm clusters (Fig. S7 in the ESM) with lattice fringes of rutile RuO_2. EDS mapping confirms that the clusters contain Ru and O elements (Fig. 2(c) and Fig. S8 in the ESM). Evidently, the RuO_2-cluster surface layer has been formed due to the dominant leaching of Sr over Ru from $SrRuO_3$ during OER (Fig. 2(d)). During the period of Sr leaching, a small part of Ru(IV) is oxidized into higher valence and dissolved into the solution (Fig. 1(b)). The dominant Sr^{2+} leaching plus minor loss of Ru^{4+} would inevitably lead to the collapse of $SrRuO_3$ lattice and split the bulk into clusters. The RuO_2 clusters are in fact the true active species for the catalysis of OER in acid.

A direct measurement of the electrocatalytic performance of the $SrRuO_3$-derived RuO_2 clusters was performed on an electrode made of pure RuO_2 clusters (see ESM for the details on harvesting of the RuO_2 clusters and the electrode preparation). The phase and composition of the harvested RuO_2 clusters have been confirmed to be pure rutile RuO_2 with XRD and free of Sr within the detection limit of ICP analysis (Table S1 in the ESM), prior to the electrode fabrication. The polarization curve of RuO_2 clusters for the catalysis of OER in 1.0 M $HClO_4$ solution (Fig. 3(a)) shows an onset overpotential of ~ 135 mV. The whole polarization curve closely resembles that of the pristine $SrRuO_3$ ceramic electrode (Fig. S9 in the ESM). The Tafel slope of 71 $mV{\cdot}dec^{-1}$ is slightly higher than that of $SrRuO_3$ ceramic (48.0 $mV{\cdot}dec^{-1}$), which is probably due to the prominent corrosion of Ru element in the latter case especially at the initial OER stage (inset of Fig. 1(b)). The overpotential required to reach 10 $mA{\cdot}cm_{geo}^{-2}$ is as low as 160 mV, coinciding well with that for the $SrRuO_3$ ceramic electrode.

The mass activity of the RuO_2 clusters is reported for the electrode with 0.5 $mg{\cdot}cm^{-2}$ loading (Fig. 3(a)). The overpotential at 50 $mA{\cdot}mg^{-1}$ is ~ 190 mV for as-prepared RuO_2 clusters, which is lowered by over 50 mV compared to the best values we could find

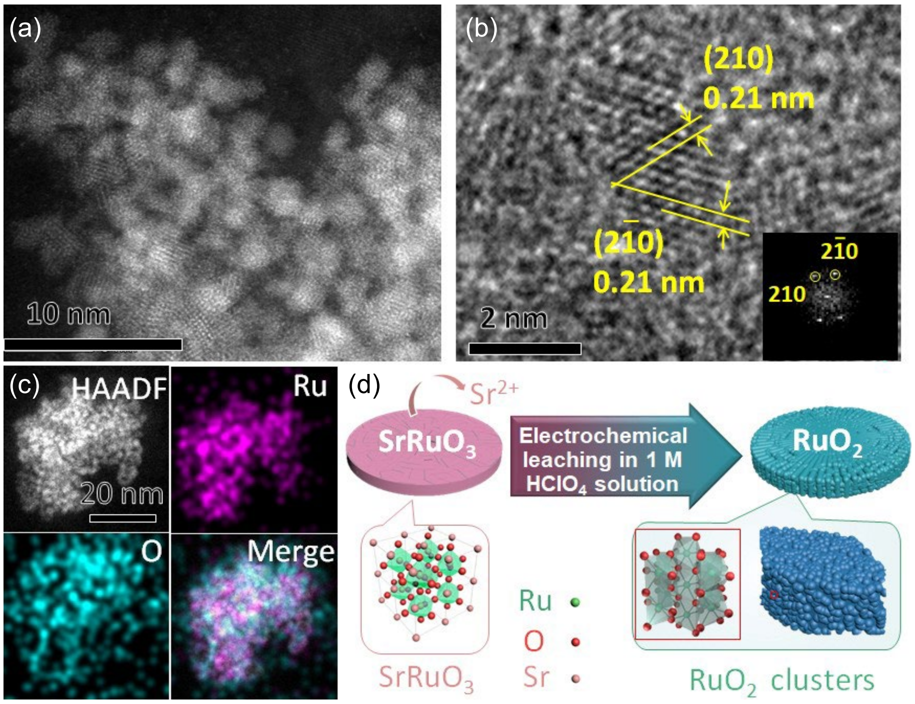

Figure 2 The structural characterization of RuO_2 clusters derived from $SrRuO_3$ ceramic: (a) HAADF-STEM image and (b) HRTEM image of powders scratched from the surface of $SrRuO_3$ ceramic electrode after 30-h CP testing (the inset shows the fast Fourier transformation of the lattice fringes of the RuO_2 clusters), revealing the formation of a surface layer of RuO_2 clusters. (c) HAADF-STEM image and element mapping. Scale bar, 500 nm. (d) Schematic illustration of formation of RuO_2 clusters via Sr leaching from bulk $SrRuO_3$ during OER in acid.

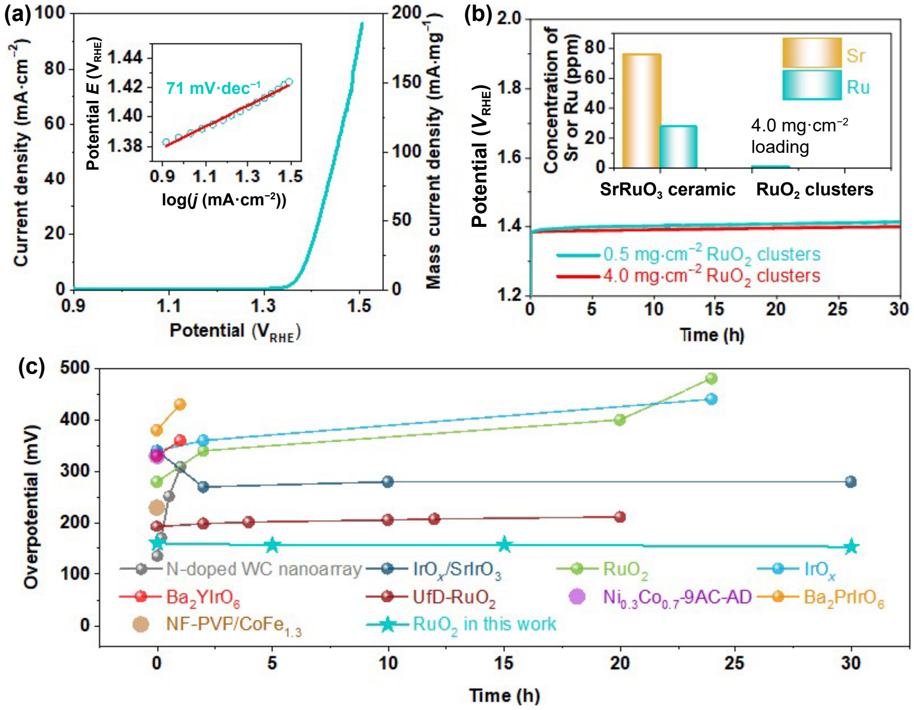

Figure 3 (a) Polarization curve for OER of as-prepared RuO_2 cluster ceramic in $HClO_4$ solution (1.0 M) at a scanning rate of 0.1 $mV\cdot s^{-1}$ and a rotating speed of 1,600 rpm (the inset is the corresponding Tafel plot). (b) Potential required to reach 10 $mA\cdot cm_{geo}^{-2}$ for $SrRuO_3$ ceramic over 30-h OER testing. (c) List of overpotentials at 10 $mA\cdot cm_{geo}^{-2}$ current density for comparing the OER performance of RuO_2 clusters with that of previously reported materials (N-doped WC nanoarray [1], $IrO_x/SrIrO_3$ [22], RuO_2 [23], IrO_x [23], Ba_2YIrO_6 [31], Ba_2PrIrO_6 [21], UfD-RuO_2 [32], $Ni_{0.3}Co_{0.7}$-9Ac-AD [20], and NF-PVP/$CoFe_{1.3}$ [29]) for OER in acidic electrolyte.

in literature for the OER catalysts in acid (Table S2 in the ESM). The specific activity of the RuO_2 clusters has been derived by normalizing the current to the BET surface area of the 0.5 $mg\cdot cm^{-2}$ loading electrode. As listed in Table S2 in the ESM, it is shown that the specific current of as-prepared RuO_2 clusters is 0.0101 $mA\cdot cm^{-2}$ at 1.4 V_{RHE}. In comparison with previously reported RuO_2 films or nanoparticles (Table S3 in the ESM), the specific current density of the RuO_2 clusters is obviously higher at 1.4 V_{RHE}.

The catalytic stability of the RuO_2 clusters for OER in acid was examined by 30-h CP measurement at a current density of 10 $mA\cdot cm_{geo}^{-2}$ (Fig. 3(b)). It is shown that at 0.5 $mg\cdot cm^{-2}$ loading, the overpotential of RuO_2-clusters starts from ~ 160 mV and then slowly increases to ~ 185 mV over 30-h testing to maintain a current density of 10 $mA\cdot cm_{geo}^{-2}$. Slight increase of the loading amount to 4.0 $mg\cdot cm^{-2}$ loading further improves the CP performance, with the overpotential at 10 $mA\cdot cm_{geo}^{-2}$ kept at ~ 160 ± 10 mV over 30 h (Fig. 3(b)). The HRTEM images of RuO_2

clusters after 30-h CP measurement (Fig. S10 in the ESM) show that their size, morphology and crystal structure are well retained. The chemical stability, measured as the material loss of RuO_2-cluster catalyst after 30-h CP testing at 10 $mA \cdot cm_{geo}^{-2}$ by ICP analysis, has been improved by nearly two orders of magnitude compared to $SrRuO_3$ ceramic (inset of Fig. 3(b) and Table S1 in the ESM), as the dominant Sr leaching in the case of $SrRuO_3$ has been avoided for the RuO_2-cluster catalyst. The chronoamperometry test was also carried out by using 1.39 V_{RHE} of driven potential (Fig. S11 in the ESM) and the results show that the current density is well retained within 15 h. It is thus shown that the RuO_2 clusters exhibit ultrahigh activity, excellent stability and durability for catalysis of OER in acid, which outperforms previously reported catalysts to our best knowledge (Fig. 3(c)).

Both extrinsic and intrinsic factors might contribute to the ultrahigh OER activity of as-derived RuO_2 clusters. Firstly, the clusters possess very large specific surface area, giving rise to a much higher density of active sites in the catalyst made of RuO_2 clusters relative to that made of micro/nano-sized RuO_2. Secondly, enlarged Jahn-Teller distortion has occurred in the RuO_2 clusters. Ru^{4+} has d^4 electronic configuration and a low-spin coordination center (Table S4 in the ESM). Its four d electrons fill three t_{2g} orbitals of which two are singly occupied (left panel in Fig. S12 in the ESM). Jahn-Teller distortion occurs in such a case, as accompanied t_{2g} orbital splitting results in reduction of the total energy (right panel in Fig. S12 in the ESM). Structural changes of the RuO_2 clusters relative to bulk RuO_2 (powders with size larger than 10 μm) were tracked with X-ray absorption fine structure spectra (Ru K-edge). The X-ray absorption near edge structure (XANES) spectra are presented in Fig. 4(a), indicating the identical chemical valence of Ru in both RuO_2 clusters and bulk. The extended X-ray absorption fine structure (EXAFS) analysis, as presented in Fig. 4(b), shows that the peaks fade fast with increasing R in the RuO_2 clusters, which is consistent with the small size of the clusters. The structure parameters of RuO_2 clusters and bulk extracted from the Ru K-edge EXAFS fitting are presented in Fig. S12 and Table S5 in the ESM. In rutile RuO_2 structure, Ru^{4+} in each RuO_6 octahedron is bonded to two axial oxygen ions at a relatively shorter distance (denoted as Ru–Ov) and four in-plane oxygen ions at a longer distance (denoted as Ru–Op). The fitting results (Table S5 in the ESM) show that Ru–Op in the clusters is lengthened by about 1.5% compared to the case of RuO_2 bulk while Ru–Ov in the clusters remains more or less the same, indicating presence of enlarged Jahn-Teller distortion in the RuO_2 clusters.

With the aid of DFT calculations, we further investigated the influence of the identified Ru–O octahedra distortion in terms of the electronic structure and intrinsic OER activity of RuO_2. To mimic Ru–O octahedra distortion as demonstrated in EXAFS fitting results (Table S5 in the ESM), we constructed the atomic structure of rutile RuO_2 with uniaxial strain applied in its c axis direction. The applied strain varies from −4% to 6% with a increment of 2%. It is shown in Table S5 in the ESM that the tensile strain elongates the Ru–O_p bond and the compressive-strain shortens Ru–O_p, while the Ru–O_v is kept almost unchanged. The tensile-strain induced Ru–O octahedra distortion shows the same type of enhanced Jahn-Teller distortion as found in the RuO_2 clusters. Then the most stable (110) surface of rutile RuO_2 was chosen to study its OER activity. By using previously established models [50] for evaluating theoretical OER activity with explicit water solvation and van der Waals interactions included [51], we investigated the reaction paths and overall OER activity as shown in Figs. S13 and S14, and Table S6–S8 in the ESM. The transition from *O to *OOH is shown to be the potential-limiting step of the overall OER processes with varied strain. It is demonstrated that for OER process, the tensile strain along c axis can effectively lower the free energy of *OOH on rutile RuO_2 surface (Fig. 4(c), and Figs. S13 and S14 in the ESM), which can be rationalized by molecular orbital theory as well [52], and thus reduce the OER overpotential. In our calculation, RuO_2 with 2% strain imposed in c axis resembles the experimental samples most in terms of RuO_6 octahedron distortion (Table S7 in the ESM), and is shown to result in a reduction of the overpotential by ~ 40 mV. The Jahn-Teller-like distortion in the octahedron of RuO_2 could delicately tune the electronic structure of RuO_2, and hence further improves the already excellent OER performance.

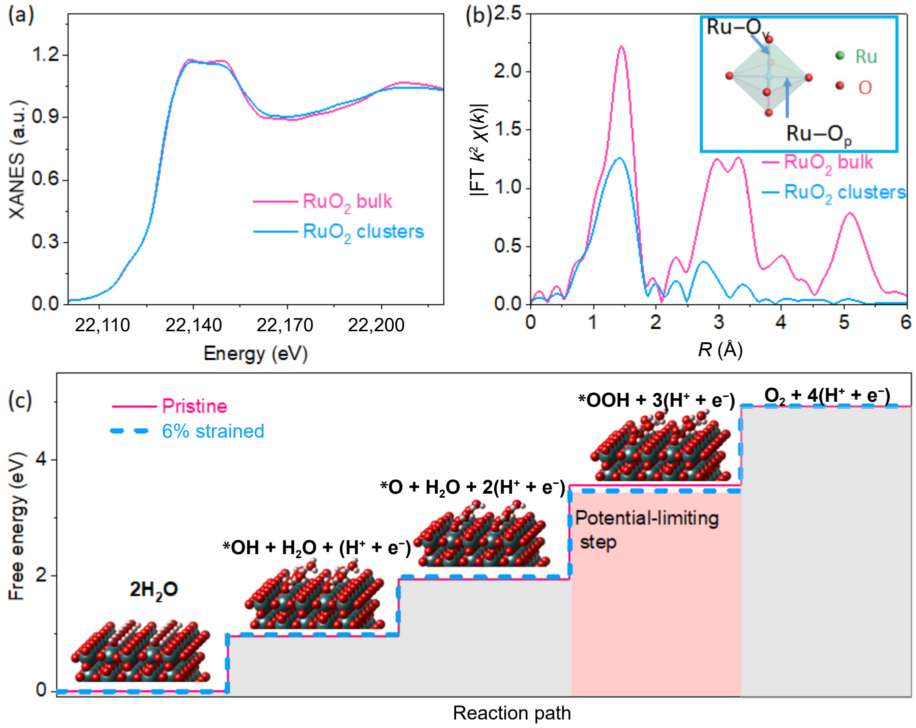

Figure 4 The EXAFS characterization of RuO_2 clusters and the DFT simulation: (a) Ru K-edge XANES spectra of RuO_2 clusters and bulk; (b) magnitude of the Fourier transforms of the k^2-weighted Ru K-edge EXAFS function; (c) free energy diagram of OER on pristine and 6%-strained RuO_2.

4 Conclusion

In summary, we show that uniform RuO_2 clusters can be derived from bulk $SrRuO_3$ via the dominant electrochemical leaching of Sr over Ru in acid, demonstrating a facile top-down strategy for synthesis of clusters from bulk material via leaching. The derived RuO_2 clusters show a stable ultralow overpotential of ~ 160 mV at 10 $mA{\cdot}cm_{geo}^{-2}$ over 30 h and are responsible for the apparent high OER performance of the $SrRuO_3$ ceramic electrode. Although the $SrRuO_3$ ceramic electrode suffers from severe material loss, the RuO_2 clusters exhibit greatly improved durability as the dominant electrochemical leaching of Sr has been avoided. The remarkably high OER activity of RuO_2 clusters originates not only from the ultrahigh specific surface area but also from the enhanced Jahn-Teller distortion in the RuO_2 clusters compared to bulk rutile RuO_2. DFT calculations have shown that the presence of enhanced Jahn-Teller distortion with Ru–O_v lengthened by about 1.5% compared to the case of RuO_2 bulk can improve the intrinsic activity of rutile RuO_2 by ~ 40 mV. The work has identified the as-derived RuO_2 clusters as robust OER catalyst in acid, and highlights the potential to obtain excellent catalysts in the cluster regime where high density of active sites and strain tuning could be envisaged.

Acknowledgements

This work was supported by the National Natural Science Foundation of China (Nos. 22022508, 51602143 and 11874036), Guangdong Natural Science Foundation for Distinguished Young Scholars (No. 2016A030306020), and the National Key Research and Development Program of China (No. 2017YFB0701600). We also thank the staffs from BL14W1 beamline of National Facility for Protein Science in Shanghai (NFPS) at Shanghai Synchrotron Radiation Facility, for assistance during data collection. Tianjin and Guangzhou Supercomputing Center is also acknowledged for allowing the use of computational resources including TIANHE-1 and TIANHE-2.

Electronic Supplementary Material: Supplementary material (the additional SEM and TEM images and the additional XRD patterns, and the corresponding electrocatalytic curves) is available in the online version of this article at https://doi.org/10.1007/s12274-021-3843-8.

References

[1] Han, N. N.; Yang, K. R.; Lu, Z. Y.; Li, Y. J.; Xu, W. W.; Gao, T. F.; Cai, Z.; Zhang, Y.; Batista, V. S.; Liu, W. et al. Nitrogen-doped tungsten carbide nanoarray as an efficient bifunctional electrocatalyst for water splitting in acid. *Nat. Commun.* **2018**, *9*, 924.

[2] Wu, G.; Chen, W. X.; Zheng, X. S.; He, D. P.; Luo, Y. Q.; Wang, X. Q.; Yang, J.; Wu, Y.; Yan, W. S.; Zhuang, Z. B. et al. Hierarchical Fe-doped NiO_x nanotubes assembled from ultrathin nanosheets containing trivalent nickel for oxygen evolution reaction. *Nano Energy* **2017**, *38*, 167–174.

[3] Gao, R.; Yan, D. P. Fast formation of single-unit-cell-thick and defect-rich layered double hydroxide nanosheets with highly enhanced oxygen evolution reaction for water splitting. *Nano Res.* **2018**, *11*, 1883–1894.

[4] Qian, M. M.; Cui, S. S.; Jiang, D. C.; Zhang, L.; Du, P. W. Highly efficient and stable water-oxidation electrocatalysis with a very low overpotential using fenip substitutional-solid-solution nanoplate arrays. *Adv. Mater.* **2017**, *29*, 1704075.

[5] Chen, G.; Zhou, W.; Guan, D. Q.; Sunarso, J.; Zhu, Y. P.; Hu, X. F.; Zhang, W.; Shao, Z. P. Two orders of magnitude enhancement in oxygen evolution reactivity on amorphous $Ba_{0.5}Sr_{0.5}Co_{0.8}Fe_{0.2}O_{3-\delta}$ nanofilms with tunable oxidation state. *Sci. Adv.* **2017**, *3*, e1603206.

[6] Chen, S.; Huang, H.; Jiang, P.; Yang, K.; Diao, J. F.; Gong, S. P.; Liu, S.; Huang, M. X.; Wang, H.; Chen, Q. W. Mn-doped RuO_2 nanocrystals as highly active electrocatalysts for enhanced oxygen evolution in acidic media. *ACS Catal.* **2020**, *10*, 1152–1160.

[7] Feng, Z. X.; Hong, W. T.; Fong, D. D.; Lee, Y. L.; Yacoby, Y.; Morgan, D.; Shao-Horn, Y. Catalytic activity and stability of oxides: The role of near-surface atomic structures and compositions. *Acc. Chem. Res.* **2016**, *49*, 966–973.

[8] Nellist, M. R.; Laskowski, F. A. L.; Lin, F.; Mills, T. J.; Boettcher, S. W. Semiconductor-electrocatalyst interfaces: Theory, experiment, and applications in photoelectrochemical water splitting. *Acc. Chem. Res.* **2016**, *49*, 733–740.

[9] Li, H. Y.; Chen, S. M.; Jia, X. F.; Xu, B.; Lin, H. F.; Yang, H. Z.; Song, L.; Wang, X. Amorphous nickel-cobalt complexes hybridized with 1T-phase molybdenum disulfide via hydrazine-induced phase transformation for water splitting. *Nat. Commun.* **2017**, *8*, 15377.

[10] He, P.; Yu, X. Y.; Lou, X. W. Carbon-Incorporated Nickel-cobalt mixed metal phosphide nanoboxes with enhanced electrocatalytic activity for oxygen evolution. *Angew. Chem., Int. Ed.* **2017**, *129*, 3955–3958.

[11] Wu, Y. Y.; Tariq, M.; Zaman, W. Q.; Sun, W.; Zhou, Z. H.; Yang, J. Ni-Co codoped RuO_2 with outstanding oxygen evolution reaction performance. *ACS Appl. Energy Mater.* **2019**, *2*, 4105–4110.

[12] Zhao, S. L.; Wang, Y.; Dong, J. C.; He, C. T.; Yin, H. J.; An, P. F.; Zhao, K.; Zhang, X. F.; Gao, C.; Zhang, L. J. et al. Ultrathin metal-organic framework nanosheets for electrocatalytic oxygen evolution. *Nat. Energy* **2016**, *1*, 16184.

[13] Zheng, Y.; Jiao, Y.; Zhu, Y. H.; Cai, Q. R.; Vasileff, A.; Li, L. H.; Han, Y.; Chen, Y.; Qiao, S. Z. Molecule-level g-C_3N_4 coordinated transition metals as a new class of electrocatalysts for oxygen electrode reactions. *J. Am. Chem. Soc.* **2017**, *139*, 3336–3339.

[14] Zhu, Y. P.; Guo, C. X.; Zheng, Y.; Qiao, S. Z. Surface and interface engineering of noble-metal-free electrocatalysts for efficient energy conversion processes. *Acc. Chem. Res.* **2017**, *50*, 915–923.

[15] Gao, R.; Yan, D. P. Recent development of Ni/Fe-based micro/nanostructures toward photo/electrochemical water oxidation. *Adv. Energy Mater.* **2020**, *10*, 1900954.

[16] Arif, M.; Yasin, G.; Luo, L.; Ye, W.; Mushtaq, M. A.; Fang, X. Y.; Xiang, X.; Ji, S. F.; Yan, D. P. Hierarchical hollow nanotubes of NiFeV-layered double hydroxides@CoVP heterostructures towards efficient, pH-universal electrocatalytical nitrogen reduction reaction to ammonia. *Appl. Catal. B:Environ.* **2020**, *265*, 118559.

[17] Arif, M.; Yasin, G.; Shakeel, M.; Fang, X. Y.; Gao, R.; Ji, S. F.; Yan, D. P. Coupling of bifunctional CoMn-layered double hydroxide@graphitic C_3N_4 nanohybrids towards efficient photoelectrochemical overall water splitting. *Chem. Asian J.* **2018**, *13*, 1045–1052.

[18] Wu, J.; Xue, Y.; Yan, X.; Yan, W. S.; Cheng, Q. M.; Xie, Y. Co_3O_4 nanocrystals on single-walled carbon nanotubes as a highly efficient oxygen-evolving catalyst. *Nano Res.* **2012**, *5*, 521–530.

[19] Dong, Q. C.; Zhang, Y. Z.; Dai, Z. Y.; Wang, P.; Zhao, M.; Shao, J. J.; Huang, W.; Dong, X. C. Graphene as an intermediary for enhancing the electron transfer rate: A free-standing Ni_3S_2@graphene@Co_9S_8 electrocatalytic electrode for oxygen evolution reaction. *Nano Res.* **2018**, *11*, 1389–1398.

[20] Ye, W.; Yang, Y. S.; Fang, X. Y.; Arif, M.; Chen, X. B.; Yan, D. P. 2D cocrystallized metal-organic nanosheet array as an efficient and stable bifunctional electrocatalyst for overall water splitting. *ACS Sustainable Chem. Eng.* **2019**, *7*, 18085–18092.

[21] Zhou, D. J.; Cai, Z.; Bi, Y. M.; Tian, W. L.; Luo, M.; Zhang, Q.; Zhang, Q.; Xie, Q. X.; Wang, J. D.; Li, Y. P. et al. Effects of redox-active interlayer anions on the oxygen evolution reactivity of NiFe-layered double hydroxide nanosheets. *Nano Res.* **2018**, *11*, 1358–1368.

[22] Zhang, M.; Zhang, J. T.; Ran, S. Y.; Qiu, L. X.; Sun, W.; Yu, Y.; Chen, J. S.; Zhu, Z. H. A robust bifunctional catalyst for rechargeable Zn-air batteries: Ultrathin NiFe-LDH nanowalls vertically anchored on soybean-derived Fe-N-C matrix. *Nano Res.* **2021**, *14*, 1175–1186.

[23] Yu, J. H.; Cheng, G. Z.; Luo, W. 3D mesoporous rose-like nickel-iron selenide microspheres as advanced electrocatalysts for the oxygen evolution reaction. *Nano Res.* **2018**, *11*, 2149–2158.

[24] Wang, L. X.; Geng, J.; Wang, W. H.; Yuan, C.; Kuai, L.; Geng, B. Y. Facile synthesis of Fe/Ni bimetallic oxide solid-solution nanoparticles with superior electrocatalytic activity for oxygen evolution reaction. *Nano Res.* **2015**, *8*, 3815–3822.

[25] Sun, K. A.; Zhao, L.; Zeng, L. Y.; Liu, S. J.; Zhu, H. Y.; Li, Y. P.; Chen, Z.; Zhuang, Z. W.; Li, Z. L.; Liu, Z. et al. Reaction environment self-modification on low-coordination Ni^{2+} octahedra atomic interface for superior electrocatalytic overall water splitting. *J. Nano Res.* **2020**, *13*, 3068–3074.

[26] Liu, G.; Gao, X. S.; Wang, K. F.; He, D. Y.; Li, J. P. Mesoporous nickel-iron binary oxide nanorods for efficient electrocatalytic water oxidation. *Nano Res.* **2017**, *10*, 2096–2105.

[27] Xue, H. Y.; Meng, A.; Zhang, H. Q.; Lin, Y. S.; Li, Z. J.; Wang, C S. 3D urchin like V-doped CoP *in situ* grown on nickel foam as bifunctional electrocatalyst for efficient overall water-splitting. *Nano Res*. **2021**, doi: 10.1007/s12274-021-3359-2.

[28] Kong, F. T.; Qiao, Y.; Zhang, C. Q.; Fan, X. H.; Kong, A. G.; Shan, Y. K. Unadulterated carbon as robust multifunctional electrocatalyst for overall water splitting and oxygen transformation. *Nano Res.* **2020**, *13*, 401–411.

[29] Guo, Z. G.; Ye, W.; Fang, X. Y.; Wan, J.; Ye, Y. Y.; Dong, Y. Y.; Cao, D.; Yan, D. P. Amorphous cobalt-iron hydroxides as high-efficiency oxygen-evolution catalysts based on a facile electrospinning process. *Inorg. Chem. Front.* **2019**, *6*, 687–693.

[30] Seh, Z. W.; Kibsgaard, J.; Dickens, C. F.; Chorkendorff, I.; Norskov, J. K.; Jaramillo, T. F. Combining theory and experiment in electrocatalysis: Insights into materials design. *Science* **2017**, *355*, eaad4998.

[31] Grimaud, A.; Diaz-Morales, O.; Han, B. H.; Hong, W. T.; Lee, Y. L.; Giordano, L.; Stoerzinger, K. A.; Koper, M. T. M.; Shao-Horn, Y. Activating lattice oxygen redox reactions in metal oxides to catalyse oxygen evolution. *Nat. Chem.* **2017**, *9*, 457–465.

[32] Gao, R.; Zhang, H.; Yan, D. P. Iron diselenide nanoplatelets: Stable and efficient water-electrolysis catalysts. *Nano Energy* **2017**, *31*, 90–95.

[33] Arif, M.; Yasin, G.; Shakeel, M.; Mushtaq, M. A.; Ye, W.; Fang, X. Y.; Ji, S. F.; Yan, D. P. Highly active sites of NiVB nanoparticles dispersed onto graphene nanosheets towards efficient and pH-universal overall water splitting. *J. Energy Chem.* **2021**, *58*, 237–246.

[34] Yao, L. H.; Zhang, N.; Wang, Y.; Ni, Y. M.; Yan, D. P.; Hu, C. W. Facile formation of 2D Co_2P@Co_3O_4 microsheets through *in-situ* toptactic conversion and surface corrosion: Bifunctional electrocatalysts towards overall water splitting. *J. Power Sources* **2018**, *374*, 142–148.

[35] Diaz-Morales, O.; Raaijman, S.; Kortlever, R.; Kooyman, P. J.; Wezendonk, T.; Gascon, J.; Fu, W. T.; Koper, M. T. M. Iridium-based double perovskites for efficient water oxidation in acid media. *Nat. Commun.* **2016**, *7*, 12363.

[36] Over, H.; Kim, Y. D.; Seitsonen, A. P.; Wendt, S.; Lundgren, E.; Schmid, M.; Varga, P.; Morgante, A.; Ertl, G. Atomic-scale structure and catalytic reactivity of the RuO_2(110) surface. *Science* **2000**, *287*, 1474–1476.

[37] Willinger, E.; Massue, C.; Schlogl, R.; Willinger, M. G. Identifying key structural features of IrO_x water splitting catalysts. *J. Am. Chem. Soc.* **2017**, *139*, 12093–12101.

[38] Wilde, P. M.; Guther, T. J.; Oesten, R.; Garche, J. Strontium ruthenate perovskite as the active material for supercapacitors. *J. Electroanal. Chem.* **1999**, *461*, 154–160.

[39] Zagalskaya, A.; Alexandrov, V. Role of defects in the interplay between adsorbate evolving and lattice oxygen mechanisms of the oxygen evolution reaction in RuO_2 and IrO_2. *ACS Catal.* **2020**, *10*, 3650–3657.

[40] Seitz, L. C.; Dickens, C. F.; Nishio, K.; Hikita, Y.; Montoya, J.; Doyle, A.; Kirk, C.; Vojvodic, A.; Hwang, H. Y.; Norskov, J. K. et al. A highly active and stable $IrO_x/SrIrO_3$ catalyst for the oxygen evolution reaction. *Science* **2016**, *353*, 1011–1014.

[41] McCrory, C. C. L.; Jung, S.; Ferrer, I. M.; Chatman, S. M.; Peters, J. C.; Jaramillo, T. F. Benchmarking hydrogen evolving reaction and oxygen evolving reaction electrocatalysts for solar water splitting devices. *J. Am. Chem. Soc.* **2015**, *137*, 4347–4357.

[42] Su, J. W.; Ge, R. X.; Jiang, K. M.; Dong, Y.; Hao, F.; Tian, Z. Q.; Chen, G. X.; Chen, L. Assembling ultrasmall copper-doped ruthenium oxide nanocrystals into hollow porous polyhedra: Highly robust electrocatalysts for oxygen evolution in acidic media. *Adv. Mater.* **2018**, *30*, 1801351.

[43] Kim, J.; Shih, P. C.; Tsao, K. C.; Pan, Y. T.; Yin, X.; Sun, C. J.; Yang, H. High-performance pyrochlore-type yttrium ruthenate electrocatalyst for oxygen evolution reaction in acidic media. *J. Am. Chem. Soc.* **2017**, *139*, 12076–12083.

[44] Kim, B. J.; Abbott, D. F.; Cheng, X.; Fabbri, E.; Nachtegaal, M.; Bozza, F.; Castelli, I. E.; Lebedev, D.; Schäublin, R.; Copéret, C. et al. Unraveling thermodynamics, stability, and oxygen evolution activity of strontium ruthenium perovskite oxide. *ACS Catal.* **2017**, *7*, 3245–3256.

[45] Lee, S. A.; Oh, S.; Hwang, J. Y.; Choi, M.; Youn, C.; Kim, J. W.; Chang, S. H.; Woo, S.; Bae, J. S.; Park, S. et al. Enhanced electrocatalytic activity via phase transitions in strongly correlated $SrRuO_3$ thin films. *Energy Environ. Sci.* **2017**, *10*, 924–930.

[46] Sahu, R. K.; Pandey, S. K.; Pathak, L. C. Valence and origin of metal-insulator transition in Mn doped $SrRuO_3$ studied by electrical transport, X-ray photoelectron spectroscopy and LSDA+*U* calculation. *J. Solid State Chem.* **2011**, *184*, 523–530.

[47] Chang, S. H.; Danilovic, N.; Chang, K. C.; Subbaraman, R.; Paulikas, A. P.; Fong, D. D.; Highland, M. J.; Baldo, P. M.; Stamenkovic, V. R.; Freeland, J. W. et al. Functional links between stability and reactivity of strontium ruthenate single crystals during oxygen evolution. *Nat. Comm.* **2014**, *5*, 4191.

[48] Lee, Y.; Suntivich, J.; May, K. J.; Perry, E. E.; Shao-Horn, Y. Synthesis and activities of rutile IrO_2 and RuO_2 nanoparticles for oxygen evolution in acid and alkaline solutions. *J. Phys. Chem. Lett.* **2012**, *3*, 399–404.

[49] Chang, S. H.; Connell, J. G.; Danilovic, N.; Subbaraman, R.; Chang, K. C.; Stamenkovic, V. R.; Markovic, N. M. Activity-stability relationship in the surface electrochemistry of the oxygen evolution reaction. *Faraday Discuss.* **2014**, *176*, 125–133.

[50] Rossmeisl, J.; Qu, Z. W.; Zhu, H.; Kroes, G. J.; Nørskov, J. K. Electrolysis of water on oxide surfaces. *J. Electroanal. Chem.* **2007**, *607*, 83–89.

[51] Briquet, L. G. V.; Sarwar, M.; Mugo, J.; Jones, G.; Calle-Vallejo, F. A new type of scaling relations to assess the accuracy of computational predictions of catalytic activities applied to the oxygen evolution reaction. *ChemCatChem* **2017**, *9*, 1261–1268.

[52] Hwang, J.; Rao, R. R.; Giordano, L.; Katayama, Y.; Yu, Y.; Shao-Horn, Y. Perovskites in catalysis and electrocatalysis. *Science* **2017**, *358*, 751–756.